nature medicine

Activation of the reward system boosts innate and adaptive immunity

Tamar L Ben-Shaanan[1,2], Hilla Azulay-Debby[1,2], Tania Dubovik[1], Elina Starosvetsky[1], Ben Korin[1,2], Maya Schiller[1,2], Nathaniel L Green[1,2], Yasmin Admon[1], Fahed Hakim[1,3], Shai S Shen-Orr[1,4,5] & Asya Rolls[1,2,5]

Positive expectations contribute to the clinical benefits of the placebo effect[1,2]. Such positive expectations are mediated by the brain's reward system[3,4]; however, it remains unknown whether and how reward system activation affects the body's physiology and, specifically, immunity. Here we show that activation of the ventral tegmental area (VTA), a key component of the reward system, strengthens immunological host defense. We used 'designer receptors exclusively activated by designer drugs' (DREADDs) to directly activate dopaminergic neurons in the mouse VTA and characterized the subsequent immune response after exposure to bacteria (*Escherichia coli*), using time-of-flight mass cytometry (CyTOF) and functional assays. We found an increase in innate and adaptive immune responses that were manifested by enhanced antibacterial activity of monocytes and macrophages, reduced *in vivo* bacterial load and a heightened T cell response in the mouse model of delayed-type hypersensitivity. By chemically ablating the sympathetic nervous system (SNS), we showed that the reward system's effects on immunity are, at least partly, mediated by the SNS. Thus, our findings establish a causal relationship between the activity of the VTA and the immune response to bacterial infection.

Despite its elusive nature, the potency of the placebo effect is recognized in modern medicine. For 50 years, clinical trials have included a placebo group to control for nonspecific effects, such as statistical errors, spontaneous recovery and patient expectations. Such expectation of clinical improvement has a key role in the placebo effect[5,6] and has been associated with activation of the brain's reward system[3,4]. It is, however, unknown whether and how activity of the brain's reward system can affect physical health, specifically immunity, and, if it does, what peripheral components mediate this interaction.

The immune system responds to psychological and cognitive factors[7,8], including positive emotions[9–14], in which the reward system has a crucial role[15,16]. Thus, we designed our study to examine whether reward system activation, which is evident in the placebo response and in positive expectation, can impact immunity. To determine the effects of the reward system on immunity, we focused on dopaminergic neurons in the VTA, a central mediator of reward-related stimuli and positive expectations[17].

To manipulate neuronal activity, we used DREADDs, which are G-protein-coupled receptors (GPCRs) that have been mutated to be activated only by an otherwise inert ligand (clozapine-*N*-oxide; CNO)[18]. These DREADDs activate endogenous downstream signal transduction pathways to augment neuronal activity[18]. To express DREADDs and a fluorescent reporter marker in VTA dopaminergic neurons, we stereotactically injected a viral vector that expresses a Cre-dependent DREADD construct (AAV8-h*Syn1*-DIO-hM3D(Gq)-mCherry) under the control of the human synapsin I (*Syn1*) promoter in mice that express *Cre* under the tyrosine hydroxylase (*Th*) promoter (which we refer to as TH-Cre mice). As a control, we infected another group of mice with a sham virus that expresses only the fluorescent reporter (**Fig. 1a**). Throughout the study, mice injected with the sham virus were used as the control group. Immunohistochemical analysis revealed that TH^+ cells in the VTA expressed the fluorescent reporter (**Fig. 1b** and **Supplementary Fig. 1**). Among these TH^+ cells, the efficiency of viral infection was 58% ± 4% (**Fig. 1c**). We verified DREADD-induced neuronal activation by analyzing the expression of c-Fos, an immediate-early activation marker, following intraperitoneal (i.p.) injection of CNO. c-Fos expression was evident in 42% ± 0.5% of DREADD-expressing cells, as compared to 3% ± 1% in control mice infected with the sham virus (**Fig. 1d**,**e**). To determine the behavioral effects of DREADD-induced VTA activation, we evaluated mouse behavior using the 'conditioned place preference' (CPP) paradigm. This assay quantifies an animal's preference for a location in which it had a subjectively positive experience[19]. Despite the low temporal resolution of DREADDs, mice in which VTA activation was induced (hereafter referred to as VTA-activated mice) showed a 31.5% ± 12.6% increased preference for the chamber in which they were injected with CNO (**Fig. 1f–h**). In addition, VTA-activated mice participated in more social interactions with cage mates (44.4% ± 12.9% increase; **Supplementary Fig. 2**), consistent with a recent report that found VTA activation increases social behavior[20]. Thus, we concluded that DREADDs were specifically expressed in VTA TH^+ neurons and that they activated the reward system in the experimental mice.

[1]Department of Immunology, Rappaport Faculty of Medicine, Technion–Israel Institute of Technology, Haifa, Israel. [2]Center of Science and Engineering of Neuronal Systems, Rappaport Faculty of Medicine, Technion–Israel Institute of Technology, Haifa, Israel. [3]Pediatric Pulmonary Unit, Rambam Health Care Campus, Haifa, Israel. [4]Faculty of Biology, Technion–Israel Institute of Technology, Haifa, Israel. [5]These authors jointly directed this work. Correspondence should be addressed to A.R. (rolls@technion.ac.il) or S.S.S.-O. (shenorr@technion.ac.il).

Received 15 January; accepted 1 June; published online 4 July 2016; doi:10.1038/nm.4133

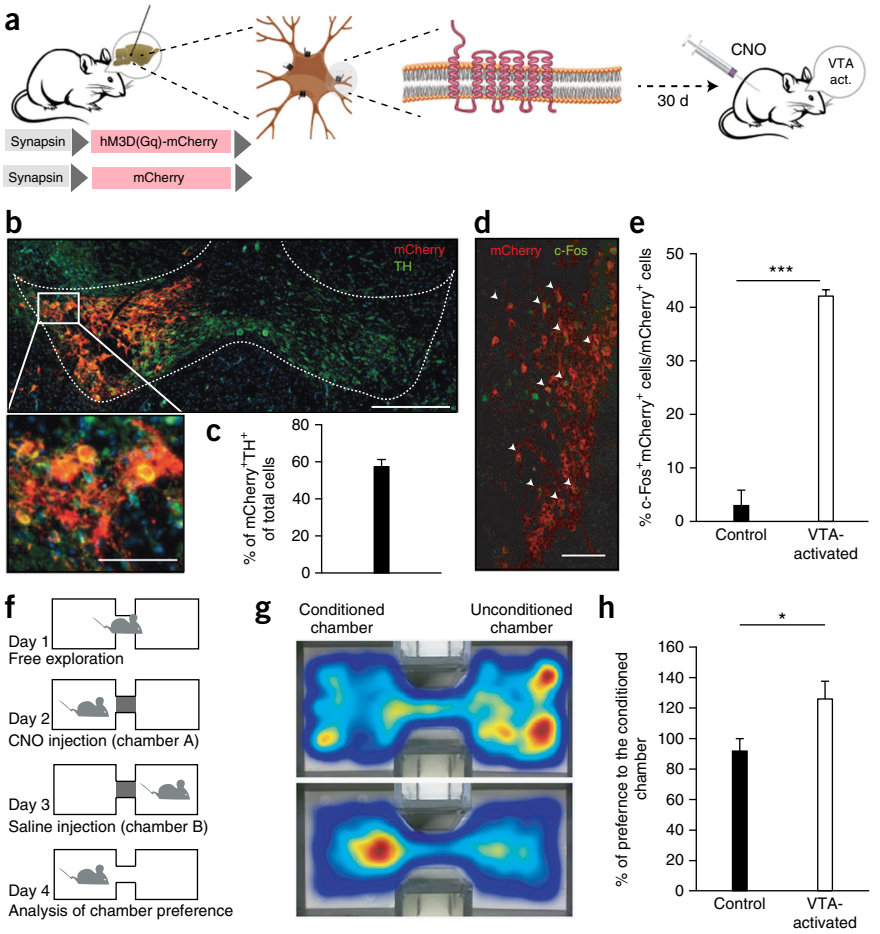

Figure 1 Activation of VTA neurons with DREADDs stimulates reward circuitry and behavioral responses. (**a**) Schematic representation of the experimental design—including a depiction of the viral constructs used for Cre-dependent expression of DREADDs and for expression of mCherry, and the representation of a DREADD on the cell-surface membrane. VTA act., activated VTA. (**b**,**c**) Representative images of a wide-angle view (top) and a higher-magnification view of the boxed area (bottom) of the virus infection site (**b**) and quantification of the fraction of mCherry$^+$TH$^+$ cells among the total number of TH$^+$ cells ($n = 3$ mice) (**c**). In **b**, dashed lines outline the VTA, as indicated in the Allen Brain Atlas depiction of the VTA. Viral expression is indicated by mCherry fluorescence (red), co-localized with the VTA TH$^+$ neurons (green). Scale bars, 0.5 mm (**b**, top) and 100 µm (**b**, bottom). (**d**,**e**) Representative images showing staining of c-Fos (green) and mCherry (red) in the VTA 90 min after activation (**d**) and quantification of c-Fos staining in virus infected cells ($n = 3$ mice per group) (**e**). In **d**, arrowheads indicate neurons co-labeled for c-Fos and mCherry. Scale bar, 100 µm. (**f**) Schematic representation of the CPP paradigm (Online Methods). (**g**,**h**) A heat map aggregating the location of all mice in the control (top) or VTA-activated (bottom) mouse group in the CPP arena during the test session (day 4) (**g**) and quantification of the proportion of time spent in the conditioned chamber on the test session (day 4) relative to that on the pre-test (day 1) ($n = 8$ mice per group) (**h**). In **g**, the color gradient indicates areas where the mice spent less time (blue) and areas where the mice spent more time (red). Arena width is 35 cm. Throughout, data are represented as mean ± s.e.m. $^*P < 0.05$, $^{***}P < 0.001$; by unpaired two-tailed Student's *t*-test.

To determine the impact of reward system activation on the immune system, we activated the VTA and screened for changes in cellular immunity. Of note, at this stage we did not introduce any direct immunological challenge. We used CyTOF, a proteomics technology that assesses cell subset abundance and protein expression at single-cell resolution[21]. We analyzed immune cells in the spleen and blood of mice 24 h after VTA activation and found small yet statistically significant (false discovery rate (FDR) of 5%) changes in functional marker expression in several cell subsets (**Supplementary Figs. 3** and **4** and **Supplementary Table 1**). We observed an increase in toll-like receptor (TLR) 4, interleukin 2 receptor alpha chain (IL2RA; also known as CD25), CD80 (also known as B7-1) and CD86 (also known as B7-2) mainly on splenic B cells, monocytes and macrophages (**Supplementary Figs. 3–5** and **Supplementary Table 1**). However, we could not identify a clear bias toward a pro- or anti-inflammatory phenotype, as serum cytokine levels, specifically those for interferon (IFN)-γ, tumor necrosis factor (TNF)-α, interleukin (IL)-4 and IL-10, were not significantly altered by VTA activation (**Supplementary Fig. 6**). Therefore, we hypothesized that the functional effect of VTA activation on the immune system might become evident only after the immune system is challenged.

To challenge the immune system, we injected VTA-activated mice and their controls with green fluorescent protein (GFP)-expressing *E. coli* by i.p. injection 24 h after VTA activation (**Fig. 2a**). We then isolated cells from the peritoneal cavity and determined their GFP levels with flow cytometry, as only cells that phagocytized the *E. coli* became GFP positive (**Supplementary Fig. 7**). We found that mononuclear CD11b$^+$GFP$^+$ cells were more abundant in the peritoneum of VTA-activated mice than in control mice (**Fig. 2b**,**c**), suggesting increased phagocytic activity in these cells following VTA activation. To confirm the increase in phagocytosis we cultured lipopolysaccharide (LPS)-stimulated splenocytes from VTA-activated mice and their controls with fluorescein isothiocyanate (FITC)-conjugated ovalbumin (OVA) (**Fig. 2d**). CD11c$^+$ dendritic cells (DCs) (**Fig. 2e**) and CD11b$^+$F4/80$^+$ macrophages (**Fig. 2f**) from VTA-activated mice had increased levels of FITC, indicating increased phagocytosis.

Next we examined whether VTA activation also affected the bactericidal properties of monocytes and macrophages. We isolated monocytes and macrophages (CD11b$^+$Ly6G$^-$) from the spleens of VTA-activated mice and their controls and cultured them with *E. coli*. We then quantified the surviving bacteria in the culture medium (**Fig. 2d**). There were fewer *E. coli* colonies in bacterial cultures that were incubated with monocytes and macrophages derived from VTA-activated mice (**Fig. 2g**,**h**) than from those cultured with monocytes and macrophages derived from the control mice. To assess the bactericidal activity *in vivo*, we performed a bacterial clearance assay. We activated the VTA and, 24 h later, intravenously (i.v.) administered *E. coli*. We analyzed the number of surviving bacteria 4 h later and found a reduced bacterial load in the liver of VTA-activated mice (**Fig. 2i**). Taken together, these findings suggest

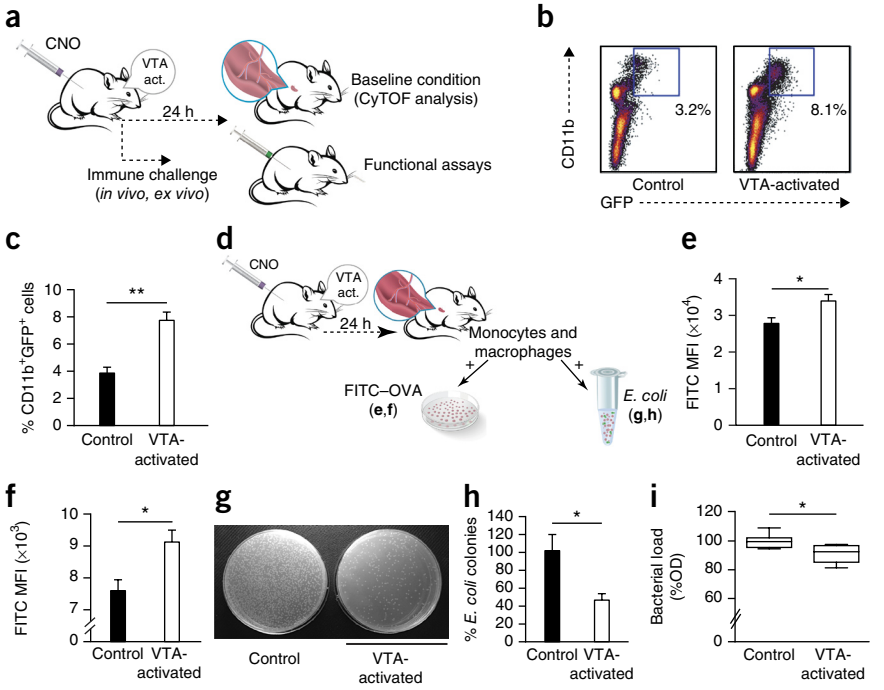

Figure 2 Activation of VTA neurons improves the innate immune response to *E.coli*. (**a**) Schematic illustration of the experimental design. (**b**,**c**) Representative dot plot of $CD11b^+GFP^+$ cells (control for GFP baseline levels, as identified in mice that were infected with nonfluorescent *E. coli*, is provided in **Supplementary Fig. 7**) (**b**) and quantification of $CD11b^+GFP^+$ cells (control, $n = 4$ mice; VTA-activated, $n = 6$ mice) (**c**). Numbers indicate the percentage of $CD11b^+GFP^+$ cells. Controls are mice infected with the sham virus and thus express only the fluorescent reporter in their VTA TH^+ neurons, i.e., there is no VTA activation. (**d**) Schematic representation of the *ex vivo* experiments. (**e**,**f**) Phagocytosis analysis using FITC-conjugated OVA in DCs ($CD11c^+$; control, $n = 4$ mice; VTA-activated, $n = 5$ mice) (**e**) and macrophages ($CD11b^+F4/80^+$; control (no VTA activation), $n = 4$ mice; VTA-activated, $n = 5$ mice) (**f**). MFI, mean fluorescence intensity. (**g**,**h**) Representative images of agar plates showing the number of *E. coli* colonies remaining after the bacterial killing assay in monocytes and macrophages ($CD11b^+F4/80^+$) isolated from VTA-activated mice and controls (**g**) and quantification of remaining *E. coli* colonies following incubation with monocytes and macrophages derived from VTA-activated or control mice ($n = 5$ mice per group) (**h**). Scale bar, 40 mm. (**i**) Bacterial load in the liver of VTA-activated mice, as determined by spectroscopy and presented as percentage of bacterial load, as compared to that in control mice ($n = 7$ mice per group). Throughout, data are represented as mean ± s.e.m. from two independent experiments. $^*P < 0.05$, $^{**}P < 0.01$; by unpaired two-tailed Student's *t*-test.

that VTA activation before the encounter with the pathogen primes the host innate immune response to infection, as manifested by the reduced bacterial load and increased phagocytic activity.

Next we tested whether activation of the reward system could also enhance the activity of the adaptive arm of the immune response. To this end, we activated the VTA and, 24 h later, challenged the

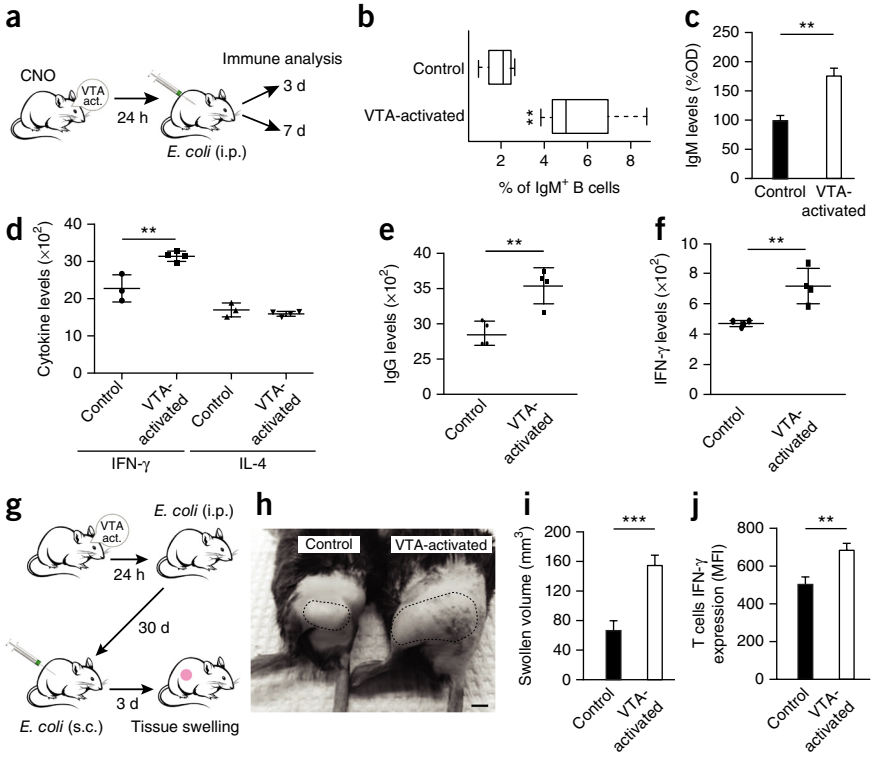

Figure 3 Activation of VTA neurons increases the adaptive immune response to *E. coli* challenge. (**a**) Schematic representation of the experimental design. (**b**) Representative example of changes in splenic B cell abundance obtained by CyTOF analysis, reported as percentage (%) of sample ($n = 5$ mice per group). Box plots denote median and inter-quantile range; whiskers are 1.5 the inter-quantile range size. (**c**) Quantification of *E. coli*–specific IgM concentrations, as measured by ELISA, in the sera of VTA-activated and control (no VTA activation) mice (results are presented as percentage optic density (%OD); $n = 6$ mice per group). (**d**) IFN-γ and IL-4 levels in splenic T cells from VTA-activated and control mice, as determined by ELISA (VTA-activated, $n = 3$ mice; control, $n = 4$ mice). (**e**) IgG expression, as determined by ELISA, on splenic B cells derived from mice 7 d after they were injected with *E. coli* and exposed *ex vivo* to *E. coli* ($n = 4$ mice per group). (**f**) IFN-γ levels in T cells derived from mice 7 d after *E. coli* injection, as determined by ELISA. Splenic T cells were isolated and then incubated *ex vivo* with *E. coli*–infected macrophages ($n = 4$ mice per group). (**g**) Schematic illustration for the DTH experimental design. (**h**,**i**) Representative image of a control mouse (infected with the sham virus) and a VTA-activated mouse, showing DTH-induced tissue swelling (as indicated by the dashed line) (**h**) and quantification of tissue swelling (control, $n = 7$ mice; VTA-activated, $n = 8$ mice) (**i**). Scale bar, 3 mm. (**j**) IFN-γ levels in T cells from lymph nodes adjacent to the *E. coli* injection site ($n = 7$ mice per group). Throughout, data are represented as mean ± s.e.m. from two independent experiments. $^{**}P < 0.01$; $^{***}P < 0.001$; by unpaired two-tailed Student's *t*-test.

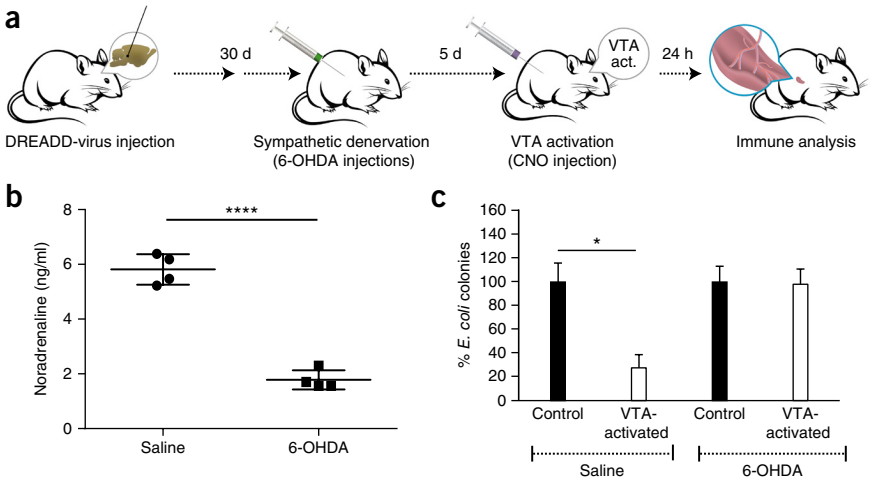

Figure 4 The effects of VTA activation on the immune system are partly mediated by the sympathetic nervous system. (**a**) Schematic depiction of the experimental design. (**b**) Analysis of norepinephrine content in the spleens of 6-OHDA-treated mice as compared to saline-injected controls ($n = 4$ mice per group). $^{****}P < 0.0001$ by unpaired two-tailed Student's *t*-test. (**c**) *Ex vivo E. coli* killing assay, as determined with four groups of mice: two with intact SNS (saline-treated VTA-activated and control) and two groups in which the SNS is disrupted (6-OHDA-treated VTA-activated and control). The number of remaining bacteria following incubation of monocytes and macrophages derived from each experimental group with *E. coli* ($n = 3$ mice per group). $^{*}P < 0.05$ by two-way analysis of variance (ANOVA). Results shown are for one of two independent experiments. Throughout, data are represented as mean ± s.e.m.

immune system by injecting *E. coli*. Because the adaptive immune response takes time to develop, we waited 3 or 7 d before euthanizing the mice (**Fig. 3a**). On day 3 following *E. coli* exposure, we found an increased abundance of IgM$^+$ B cells (CD45R$^+$CD79b$^+$IgM$^+$) in the spleen (**Fig. 3b**) and an 86% increase in *E. coli*–specific serum IgM antibodies in VTA-activated mice, as compared to those in controls (**Fig. 3c**). We also found an increase in intracellular expression of the pro-inflammatory cytokine IFN-γ (but not IL-4) in CD4$^+$ T cells that were derived from the spleen of VTA-activated mice (**Fig. 3d**). However, on day 7 following *E. coli* exposure, we could not identify any differences in the expression of functional markers between splenocytes derived from VTA-activated and control mice (**Supplementary Fig. 8**). Nevertheless, after we re-exposed these splenocytes to *E. coli ex vivo*, we found a significant increase in the levels of IgG on the cell surface of B cells (**Fig. 3e**) and of intracellular expression of IFN-γ on T cells derived from the VTA-activated mice (**Fig. 3f**). These findings suggested that VTA activation affected the reaction to the pathogen after re-exposure. We further validated this effect *in vivo* by testing the delayed-type hypersensitivity (DTH) response. In this assay, we activated the VTA, and, 24 h later, inoculated the mice by i.p. injection with heat-killed *E. coli*. Thirty days later, we re-exposed the mice to heat-killed *E. coli* subcutaneously (s.c.) and monitored tissue swelling as a proxy for local immune activity (**Fig. 3g**). Of note, although we activated the VTA only before the initial exposure to the pathogen, VTA-activated mice demonstrated a volume of swelling twice that of controls after re-exposure to *E. coli* 30 d later (**Fig. 3h**,**i**). Moreover, IFN-γ expression was elevated in CD4$^+$ T cells from the lymph nodes draining the infected area of the VTA-activated mice (**Fig. 3j**). Taken together, these findings indicate that VTA activation strengthens both the innate and adaptive immune responses to the pathogen.

Activation of TH$^+$ neurons in the VTA induces a local release of dopamine[20,22]. Dopamine does not, however, cross the blood-brain barrier (BBB)[23], thus raising the question of how the signal from the reward system is conveyed to the immune system. To address this question, we focused on the sympathetic nervous system (SNS), which innervates all lymphoid organs[24], regulates immune activity[25] and has been shown to be affected by VTA activity[26]. We used 6-hydroxydopamine (6-OHDA) to chemically ablate peripheral catecholaminergic neurons of the SNS (as 6-OHDA does not cross the BBB[27]) in DREADD-expressing mice and their controls (resulting in 69.4% reduction in splenic norepinephrine levels **Fig. 4a**,**b**). We then activated the VTA of the sympathectomized mice and, 24 h later, isolated the splenocytes for CyTOF and functional analyses. In the absence of an intact SNS, CyTOF did not reveal any significant impact of VTA activation on the immune system (CD45$^+$ cells) (**Supplementary Fig. 9**). We also did not find any significant effect of VTA activation on the antibacterial activity of monocytes and macrophages after the SNS was impaired (**Fig. 4c**). Thus, although we cannot exclude the involvement of additional pathways, especially endocrine mechanisms, our data indicate that the signal from the brain's reward system to the immune system is mediated, at least in part, via the SNS.

In conclusion, we used direct neuronal manipulation to establish a causal relationship between the brain's reward system and immunity. We show that activation of the reward system increases the primary antibacterial immune response, as well as the immune response after pathogen re-exposure. These findings are in line with pharmacological and lesion studies that implicate the reward system in immune activity[28,29]. On the basis of our data, we speculate that this reward-system-driven enhancement of antibacterial immunity might be beneficial in natural contexts that are known to activate the VTA but which might also increase the likelihood of exposure to pathogens (such as feeding or mating behaviors)[30,31]. Although the use of DREADDs for VTA activation enabled us to establish its causal effects on the immune system, it does not fully mimic naturally occurring reward conditions, and further studies will be required to determine the effects of naturally occurring reward responses on immunity.

The placebo response is a powerful manifestation of the connection between positive emotions, reward system activation and physical well-being. Reward system activation is evident during the placebo response in humans[3,4], but it is mostly associated with the psychological aspects of placebo[32]. Our study, which connects reward system activity with the immune response, may shed new light on the nature of the placebo effect and suggests a neuronal mechanism by which positive expectations have an effect on peripheral immunity.

METHODS

Methods and any associated references are available in the online version of the paper.

Note: Any Supplementary Information and Source Data files are available in the online version of the paper.

ACKNOWLEDGMENTS

We would like to thank A. Ziv-Kenet for his help with CyTOF data analysis, A.D. Eban-Rothchild, C. Tourino, D. Melamed, N. Karin, G. Wildbaum, R. Hershberg and M. Rahat for helpful discussions, A. Mor, F. Zaknoon, J. Jammal, S. Yaron and S. Katz for their help with bacterial experiments, Y. Posen, G. Ginzburg and E. Reisin-Tzur for editing the paper, H. Amitay for her help with the behavioral analysis, and O. Goldberger and the Biomedical core facility at the Technion Faculty of Medicine for technical support. This research was supported by the FP-7-CIG grant 618654 (A.R.), the Israel Science Foundation (ISF) grants 1862/15 (A.R.) and 1365/12 (S.S.S.-O.), the Technion V.P.R. Fund–Malat Family (A.R.), the Adelis Foundation (A.R.) and the Rappaport Institute of Biomedical Research (S.S.S.-O.).

AUTHOR CONTRIBUTIONS

T.L.B.-S. designed and carried out all of the experiments, interpreted the results and wrote the manuscript; H.A.-D. contributed to the experimental design, carried out experiments, contributed to data analysis and to the manuscript; T.D. and E.S. designed, performed and analyzed the CyTOF experiments and contributed to the manuscript; B.K. and M.S. contributed to the experimental design and execution of the experiments, contributed to analysis of the results and contributed to the manuscript; N.L.G. contributed to the interpretation of the results and the writing the manuscript; Y.A. contributed to the CyTOF data analysis; F.H. contributed to the experimental design and data interpretation; S.S.S.-O. designed and analyzed the CyTOF experiments, contributed with the interpretation of results and wrote the manuscript; and A.R. conceived the project, contributed to the experimental design and the interpretation of results, and wrote the manuscript.

COMPETING FINANCIAL INTERESTS

The authors declare no competing financial interests.

1. Howick, J. *et al.* Placebo use in the United Kingdom: results from a national survey of primary care practitioners. *PLoS One* **8**, e58247 (2013).
2. Tilburt, J.C., Emanuel, E.J., Kaptchuk, T.J., Curlin, F.A. & Miller, F.G. Prescribing 'placebo treatments': results of national survey of US internists and rheumatologists. *BMJ* **337**, a1938 (2008).
3. de la Fuente-Fernández, R. *et al.* Expectation and dopamine release: mechanism of the placebo effect in Parkinson's disease. *Science* **293**, 1164–1166 (2001).
4. Scott, D.J. *et al.* Placebo and nocebo effects are defined by opposite opioid and dopaminergic responses. *Arch. Gen. Psychiatry* **65**, 220–231 (2008).
5. Benedetti, F., Carlino, E. & Pollo, A. How placebos change the patient's brain. *Neuropsychopharmacology* **36**, 339–354 (2011).
6. Walach, H. Placebo controls: historical, methodological and general aspects. *Phil. Trans. R. Soc. Lond. B* **366**, 1870–1878 (2011).
7. D'Acquisto, F., Rattazzi, L. & Piras, G. Smile—it's in your blood! *Biochem. Pharmacol.* **91**, 287–292 (2014).
8. Segerstrom, S.C. & Miller, G.E. Psychological stress and the human immune system: a meta-analytic study of 30 years of inquiry. *Psychol. Bull.* **130**, 601–630 (2004).
9. Barak, Y. The immune system and happiness. *Autoimmun. Rev.* **5**, 523–527 (2006).
10. Eisenberger, N.I. & Cole, S.W. Social neuroscience and health: neurophysiological mechanisms linking social ties with physical health. *Nat. Neurosci.* **15**, 669–674 (2012).
11. Fredrickson, B.L. *et al.* A functional genomic perspective on human well-being. *Proc. Natl. Acad. Sci. USA* **110**, 13684–13689 (2013).
12. Mittwoch-Jaffe, T., Shalit, F., Srendi, B. & Yehuda, S. Modification of cytokine secretion following mild emotional stimuli. *Neuroreport* **6**, 789–792 (1995).
13. Segerstrom, S.C. & Sephton, S.E. Optimistic expectancies and cell-mediated immunity: the role of positive affect. *Psychol. Sci.* **21**, 448–455 (2010).
14. Segerstrom, S.C., Taylor, S.E., Kemeny, M.E. & Fahey, J.L. Optimism is associated with mood, coping and immune change in response to stress. *J. Pers. Soc. Psychol.* **74**, 1646–1655 (1998).
15. Nieh, E.H., Kim, S.Y., Namburi, P. & Tye, K.M. Optogenetic dissection of neural circuits underlying emotional valence and motivated behaviors. *Brain Res.* **1511**, 73–92 (2013).
16. Russo, S.J. & Nestler, E.J. The brain reward circuitry in mood disorders. *Nat. Rev. Neurosci.* **14**, 609–625 (2013).
17. Schultz, W. Updating dopamine reward signals. *Curr. Opin. Neurobiol.* **23**, 229–238 (2013).
18. Armbruster, B.N., Li, X., Pausch, M.H., Herlitze, S. & Roth, B.L. Evolving the lock to fit the key to create a family of G-protein-coupled receptors potently activated by an inert ligand. *Proc. Natl. Acad. Sci. USA* **104**, 5163–5168 (2007).
19. Huston, J.P., Silva, M.A., Topic, B. & Müller, C.P. What's conditioned in conditioned place preference? *Trends Pharmacol. Sci.* **34**, 162–166 (2013).
20. Gunaydin, L.A. *et al.* Natural neural projection dynamics underlying social behavior. *Cell* **157**, 1535–1551 (2014).
21. Bendall, S.C. *et al.* Single-cell mass cytometry of differential immune and drug responses across a human hematopoietic continuum. *Science* **332**, 687–696 (2011).
22. Gratton, A., Hoffer, B.J. & Gerhardt, G.A. Effects of electrical stimulation of brain reward sites on release of dopamine in rat: an *in vivo* electrochemical study. *Brain Res. Bull.* **21**, 319–324 (1988).
23. Connolly, B.S. & Lang, A.E. Pharmacological treatment of Parkinson disease: a review. *J. Am. Med. Assoc.* **311**, 1670–1683 (2014).
24. Elenkov, I.J., Wilder, R.L., Chrousos, G.P. & Vizi, E.S. The sympathetic nerve—an integrative interface between two supersystems: the brain and the immune system. *Pharmacol. Rev.* **52**, 595–638 (2000).
25. Koopman, F.A. *et al.* Restoring the balance of the autonomic nervous system as an innovative approach to the treatment of rheumatoid arthritis. *Mol. Med.* **17**, 937–948 (2011).
26. Nakamoto, T. *et al.* Co-activation of renal sympathetic neurons and somatic motor neurons by chemical stimulation of the midbrain ventral tegmental area. *J. Appl. Physiol.* **110**, 1342–1353 (2011).
27. Kostrzewa, R.M. & Jacobowitz, D.M. Pharmacological actions of 6-hydroxydopamine. *Pharmacol. Rev.* **26**, 199–288 (1974).
28. Lacosta, S., Merali, Z., Zalcman, S. & Anisman, H. Time-dependent *in vivo* mesolimbic dopamine variations following antigenic challenge. *Brain Res.* **664**, 225–230 (1994).
29. Saurer, T.B., Ijames, S.G. & Lysle, D.T. Evidence for the nucleus accumbens as a neural substrate of heroin-induced immune alterations. *J. Pharmacol. Exp. Ther.* **329**, 1040–1047 (2009).
30. Balfour, M.E., Yu, L. & Coolen, L.M. Sexual behavior and sex-associated environmental cues activate the mesolimbic system in male rats. *Neuropsychopharmacology* **29**, 718–730 (2004).
31. Hajnal, A., Smith, G.P. & Norgren, R. Oral sucrose stimulation increases accumbens dopamine in the rat. *Am. J. Physiol. Regul. Integr. Comp. Physiol.* **286**, R31–R37 (2004).
32. Enck, P., Benedetti, F. & Schedlowski, M. New insights into the placebo and nocebo responses. *Neuron* **59**, 195–206 (2008).

ONLINE METHODS

Mice. We used male adult (10–12 weeks of age; 20–25 g) TH-Cre mice (B6.Cg-Tg(*Th-Cre*)1Tmd/J; Jackson Laboratory) in all experiments. Mice were maintained under specific-pathogen-free (SPF) conditions on a 12 h light: 12 h dark cycle (lights on at 07:00). All experiments were performed in accordance with the National Institutes of Health Guide for the Care and Use of Laboratory Animals[33]. All procedures and protocols were approved by the Technion Administrative Panel of Laboratory Animal Care. Throughout, mice were randomly assigned to the experimental groups. A sample size of three to eight mice per group was based on the feasibility of the experimental design.

Stereotactic injection. Mice were randomly divided between two experimental groups and anesthetized with a ketamine–xylazine mixture (ketamine 80 mg per kg body weight (mg/kg); xylazine 15–20 mg/kg; Sigma-Aldrich) in sterile saline solution (0.9% NaCl) before being fixed in the stereotactic frame (Stoelting). An adeno-associated virus 8 (AAV8)-based construct (Vector Core at the University of North Carolina) was used to induce Cre-dependent DREADD expression (AAV8-hSyn-DIO-hM3D(Gq)-mCherry) in TH^+ cells expressing Cre, by injection of 0.7 µl into the right VTA region (anterior–posterior −3.2 mm; medial–lateral 0.48 mm; dorsal–ventral 4.7 mm). Control mice were injected with a sham AAV8-hSyn-DIO-mCherry construct, which lacks the information for DREADD. We waited for 30 d after surgery to assure the expression of DREADDs and to avoid analyzing the immediate immune response that could be induced by the virus injection. Stereotaxic injection sites were verified by immunohistochemistry, and only mice with at least 50% of their TH^+ cells co-expressing mCherry were included in the study. We observed that 3% ± 0.8% of $mCherry^+$ cells did not show clear TH staining, consistent with the recent finding by Lammel *et al.*[34] that TH-Cre mice have some nonspecific targeting to neurons that express *Th* mRNA but are not typical dopaminergic neurons. Therefore, we refer to our DREADD manipulation of the TH^+ cells as VTA activation.

Behavioral procedure. All behavioral tests were conducted during the same circadian period. The conditional place preference (CPP) test was performed in a rectangular cage with two chambers (25 cm × 25 cm each), with a corridor (5 cm × 5 cm) connecting the two chambers. The chambers differed in their visual cues and are designed so that mice will have no bias for a particular chamber. The CPP paradigm consisted of four sessions over 4 d and was conducted 30 d after the stereotactic injection of the virus (**Fig. 1f**). On day 1, individual mice were placed in the connecting corridor (in the same direction) and were allowed to freely explore the entire apparatus for 15 min (pre-test). On day 2, the mice were intraperitoneally (i.p.) injected with CNO (2.5 mg/kg; Sigma-Aldrich) in sterile saline in order to activate the VTA neurons. Then, the mice were confined to one of the chambers for 30 min. On day 3, the mice were injected with sterile saline and confined to the other chamber for 30 min. On day 4, the mice were placed in the corridor and were allowed to freely explore the entire apparatus for 15 min (post-test). To calculate the level of preference, the relative time (%) the mouse spent during the post-test period in the conditioned chamber (the chamber where it received the CNO injection) was divided by the relative time (%) the mouse spent in this chamber during the pre-test period (post/pre ratio). Of note, in all experiments, mice in both groups were injected with CNO to control for the potential effects of CNO, which in mice does not convert to clozapine[35]. The analysis was performed automatically using EthoVision software.

Social behavior analysis was done in the home cages (six mice per cage). We analyzed the number of social interactions of each mouse with his cage mates, using video recording. We monitored the number of these interactions before CNO injection and 30 min after CNO injection. Scoring of the social interactions was preformed manually for 10 min in each analysis session. An interaction was considered as any physical encounter between two mice. Three independent researchers, blind to the identity of the mice, scored the videos. Data is reported as percentage change in social interactions following CNO injection as compared to that in control-treated mice.

Tissue preparation and immunohistochemistry. Validation of the virus injection site, evaluation of DREADD expression and c-Fos analysis were performed by immunohistochemistry. Mice were euthanized, and their brains were fixed in 4% paraformaldehyde (PFA) for 48 h and cryoprotected in 30% sucrose solution (48 h). Coronal cryosections from the midbrain were sliced at 12-µm thickness and mounted on super-frost slides (Fisherbrand). The tissues were stained for TH with mouse anti-TH (1:200; Millipore, MAB318), and the proportion of DREADD-expressing cells ($mCherry^+$) out of the total TH^+ cells in the VTA was evaluated (minimum 1,500 cells). To evaluate c-Fos expression, mice were sacrificed 90 min after CNO injection and treated as described above. Fixed sections were stained with rabbit anti-c-Fos antibodies (1:100; Calbiochem, PC38). We calculated the proportion of the $c\text{-}Fos^+$ cell nuclei from the total number of DREADD-expressing cells. All images were taken as *z*-stack fluorescent 20× magnification images using an LSM 700 confocal microscope (Carl Zeiss Inc.). The quantification of double-positive cells was performed by using Imaris Software. All tissue preparations were done by investigators who were blinded to the sample identity.

Mass cytometry measurement and analysis. Two weeks following the behavioral testing, mice were injected i.p. with CNO and anesthetized 24 h thereafter. Spleens and blood samples were collected. Spleens were dissociated into single-cell suspensions in 2% FBS in PBS (Biological Industries, IL) and mesh-filtered to remove clumps and debris. Blood samples were collected into heparin-coated sterile test tubes. Cell suspensions were treated with red blood cell lysis buffer (BD Biosciences, NJ, USA), and cells (2×10^6) from each tissue were stained (1 h; room temperature) with a mixture of metal-tagged antibodies (complete list of antibodies and their catalog numbers is provided in **Supplementary Table 2**). All antibodies were validated by the manufacturers for flow application (as indicated on the manufacturer's datasheet, available online) and were conjugated by using the MAXPAR reagent (Fluidigm Inc.). Rhodium and iridium intercalators were used to identify live and dead cells. For the barcoding experiment, we used palladium barcoding (Fluidigm Inc.) according to the manufacturer's instructions. Cells were washed twice with PBS, fixed in 1.6% formaldehyde (Sigma-Aldrich; 1 h), washed again in ultrapure water and subjected to CyTOF mass cytometry analysis on a CyTOF I machine (Fluidigm). Cell events were acquired at approximately 500 events/s. In the non-barcoded experiment, VTA-activated and control samples were assayed in differing order between the experiments to overcome potential differences in machine sensitivity. We validated staining reliability for the main markers on gated live-cell populations (**Supplementary Fig. 10**). Although marker staining was low for many markers, we noted cell-specific expression patterns across cell populations for both VTA-activation affected (**Supplementary Fig. 11**) and non-affected markers (**Supplementary Fig. 12**). In addition, we spiked each sample with internal metal-isotope bead standards for sample normalization by CyTOF software (Fluidigm Inc.). Data processing and gating out of dead cells and normalization beads was done on the Cytobank website (http://www.cytobank.org). To account for intra-run declines in mean marker intensity over time, we performed a within-sample-over-time normalization step by using a running window to adjust mean marker intensity throughout each individual run, such that the mean expression over time was equal to that measured at the beginning of the run. Data was transformed using an arcsinh (×/5) transformation.

Analysis of CyTOF data. *Citrus.* Cell subset abundance and functional marker expression in VTA-activated and control mice were compared by using the Citrus algorithm[36] (Citrus V0.8, code available through GitHub (https://github.com/nolanlab/citrus)). Briefly, Citrus analysis consists of the following. First, FCS files of normalized, 'live cell/no beads' samples are each randomly sampled for *N* single cell events (see below for details on how cell numbers sampled in each condition were chosen). Second, collected single-cell events are pooled and iteratively hierarchically clustered based on similarity of expression of subsets of the measured channels. This procedure yields overlapping clusters with the largest cluster being one encompassing all of the sampled events. Third, the pooled data set is split back into its constitutive samples, and the relative abundance of cells in each cluster is computed, as well as the median expression of each functional marker in each cluster. Only clusters whose abundance in one or more of the measured samples is greater than some lower-bound *P* values are considered for downstream differential analysis. Fourth, to

determine differences in cell subset abundances or functional marker medians expression, we used the SAM algorithm in Citrus, which assesses false discovery rate by permutations. We set *P* to 1% of sample in all conditions tested and *N* to 40 K in the case of the day 3 experiments following *E. coli* challenge and 6-OHDA experiments, as well as in one of the baseline experiments. To avoid biased sampling of samples with a lower number of events, we set the *N* in these experiments to a lower value of 20 K and 15 K cells, respectively, although removing the samples with a lower number of events and sampling 40 K from the remaining samples yielded qualitatively similar results. To assess reproducibility, we analyzed each batch separately and then compared the results of the independently analyzed batches. Abundance and median differential analysis were performed separately due to multiple-hypothesis correction considerations. Furthermore, we limited testing of functional marker group differences to clusters or cell populations expressing the marker. To do so in an unbiased manner (for each marker), we averaged the expression of the marker across all samples to yield a per cluster characteristic marker expression profile. Building on the concept of 'probability of expression' (POE) from gene expression[37], we modeled the experiment-wide background distribution of marker expression as two distributions, one positive and one negative. We computed a POE for each functional marker across all clusters, based on the first moment distance of the within-cluster single-cell marker expression from the negative background distribution. Group difference analysis was restricted to those Citrus clusters whose distribution was significantly different from that of the negative background (by Wilcoxon test) and were considered to be expressing the functional marker. Manual inspection of Citrus output was used to identify the closest known gross-cell type, matching the 23-combination clustering marker panel. We analyzed $CD45^+$ cells exclusively and characterized cell clusters using standard cell subset definitions: B cells ($CD45R^+CD79b^+$), $CD8^+$ T cells ($TCR\text{-}\beta^+CD8^+$), $CD4^+$ T cells ($TCR\text{-}\beta^+CD4^+$), NK cells ($NK1.1^+CD49b^+$), granulocytes ($CD11b^+Gr1^+$), monocytes and macrophages ($CD11b^+CD14^+F4/80^+$) and DCs ($CD11c^+$). In all conditions, we report cluster marker differences at a false discovery rate (FDR) of 10%, but, to maintain strict criteria for reproducibility, we limit our discussion to cell subsets in which differences were observed repeatedly in multiple clusters and replicated in all three repeats of the experiment (two non-barcoded and one barcoded analysis).

ViSNE analysis. This was performed on raw CyTOF data on the Cytobank database.

Manual gating. The raw CyTOF data was normalized to the calibration beads and gated for live cells. Then we applied manual gating based on the following parameters: B cells: $CD45R^+CD79b^+$; $CD8^+$ T cells: $TCR\text{-}\beta^+CD8^+$; $CD4^+$ T cells: $TCR\text{-}\beta^+CD4^+$; monocytes and macrophages: $CD11b^+F4/80^+$ and DCs: $CD11c^+$. On these gated populations, we determined the median marker intensity for the following markers: CD25, CD86, CD80, TLR4, CD115, MHCII (**Supplementary Fig. 10**).

Effect validation by flow cytometry. We validated the changes detected on monocytes and macrophages by Citrus, using flow cytometry (**Supplementary Fig. 13**).

Flow cytometry. Cells (10^6) were incubated with antibodies for 30 min at 4 °C, then washed with FACS staining buffer (PBS containing 1% bovine serum albumin and 0.05% sodium azide). The following monoclonal antibodies (mAbs) were used: Pacific Blue–conjugated anti-CD3 (BioLegend, 100334), APC-conjugated anti-CD4 (BioLegend, 100412), Alexa-Fluor-488-conjugated anti-CD8 (BioLegend, 100732), PerCP-conjugated anti-CD11b (BioLegend, 101230), APC-conjugated anti-F4/80 (BioLegend, 123116), PE–Cy7-conjugated anti-CD11c (BioLegend, 117318), PE-conjugated anti-IL-4 (BioLegend, 504104), PE–Cy7-conjugated anti-IFN-γ (BioLegend, 505826), PE–Cy7-conjugated anti-CD25 (BioLegend, 102016), Brilliant Violet 605–conjugated anti-CD115 (BioLegend, 135517), biotin-conjugated anti-TLR4 (BioLegend, 117603; together with Alexa-Fluor-488-conjugated streptavidin; Jackson, 016-540-084), PE-conjugated anti-CD80 (BioLegend, 104708), biotin-conjugated anti-CD86 (BioLegend, 105004; together with PerCP-conjugated streptavidin; Jackson, 016-120-84). All antibodies were validated by the manufacturers for flow application, as indicated on the manufacturer's website. For extracellular staining alone the samples were resuspended in 400 µl of 1% PFA and analyzed by flow cytometry. For intracellular cytokine analysis, the cells were first stained extracellularly as described above, fixated and permeabilized with BD Cytofix/Cytoperm Kit, and stained with intracellular antibodies. Samples were analyzed with an LSR Fortessa cell analyzer and FACSDiva software.

***In vivo E. coli* phagocytosis.** Mice expressing the virus (DREADDs and control) were injected (i.p.) with CNO. Twenty four hours later, mice were injected with GFP-expressing *E. coli* (MG165K12; 8×10^8 colony-forming units (c.f.u.)/mouse; i.p.). After 2 h, peritoneal lymphocytes were collected by peritoneal lavage. For peritoneal lavage, mice were killed, and their skin was cleaned with 70% ethanol. Then, 5 ml ice-cold PBS containing 1% FBS was injected into the peritoneum, followed by gentle massage to distribute the lavage fluid throughout the peritoneal cavity. Fluid was collected using a 5-ml syringe, and cells were washed twice in FACS staining buffer. To identify the monocytes that phagocytized the fluorescent bacteria, we labeled the extracted cells with PerCP-conjugated anti-CD11b antibody and analyzed them by flow cytometry as described above.

OVA–FITC phagocytosis assay. Splenocytes (10^6) from VTA-activated mice and their controls (whose VTA was not activated) were taken 24 h after CNO administration and incubated with OVA–FITC (Molecular Probes, 0.25 mg/ml) and LPS (20 ng/ml) for 4 h to allow phagocytosis of the FITC-conjugated ovalbumin. The cells were washed with cold FACS staining buffer and stained with the following antibodies: PerCP-conjugated anti-CD11b, APC-conjugated anti-F4/80 and PE–Cy7-conjugated anti-CD11c. Stained cells were analyzed by flow cytometry.

***Ex vivo E. coli* killing assay.** To evaluate the antibacterial efficiency of spleen monocytes, we performed an *ex vivo* killing assay. Splenocytes from VTA-activated mice and their controls (whose VTA was not activated) were extracted 24 h after i.p. injection with CNO. For monocyte enrichment, we used negative selection (EasySep mouse monocyte enrichment kit; Stemcell Technologies). Enriched monocytes were co-cultured with *E. coli* bacteria at a 1:12 ratio (RPMI medium (Biological Industries) containing 10% FBS; 37 °C; 4 h). Monocytes were then lysed (0.1% Triton X-100; Sigma-Aldrich), and the lysates were diluted 1:1,000 in PBS. The diluted medium was plated on Petri dishes with agar-containing medium and incubated overnight at 37 °C; the remaining bacteria colonies were then quantified.

***In vivo E. coli* injection.** 24 h following CNO injection, VTA-activated mice and their controls (whose VTA was not activated) were injected by i.p. injection with 5×10^6 c.f.u. of heat-killed *E. coli* (heated for 1 h at 80 °C) in 150 µl of sterile PBS. The mice were sacrificed 3 d later, and their blood and spleens were collected. In a clearance assay, the mice were similarly injected i.v. with *E. coli* (10^5 c.f.u.), and 4 h later we extracted their livers. The livers were gently homogenized and centrifuged (1,200 r.p.m.). Then, we sampled the remaining fluid for bacteria concentration by spectrophotometry (Infinite 200 PRO, TECAN).

Measurement of serum cytokine levels and *E. coli*–specific IgM antibodies. VTA-activated and control (whose VTA was not activated) mice were treated with CNO and, 24 h later, anesthetized with ketamine–xylazine. We collected blood by cardiac puncture, allowed it to clot at room temperature for 60 min and centrifuged it at 400*g* for 10 min to collect serum for analysis using standard ELISA kits for TNF-α, IFN-γ, IL-10 and IL-4 (PeproTech). Levels of IgM antibodies specific to *E. coli* were determined by using direct ELISA as described by Heller *et al.*[38]. Briefly, we sonicated heat-killed *E. coli* at a concentration of 10^8 c.f.u./ml using Vibra-Cell VCX 750 Sonicator (Sonics & Materials; 15 cycles, each cycle lasting 10 s with a 10-s interval). The sonicated bacterial medium was diluted in PBS (×100) and used to coat 96-well Immunoplates (Nunc), which were then washed and plated with the serum (diluted 1:1,000). Biotinylated goat anti-mouse IgM (1:2,000, SouthernBiotech) followed by streptavidin-conjugated to horseradish peroxidase (HRP) (1:5,000, Jackson) and TMB substrate (Santa Cruz) were used for detection. Plates were read in Zenyth 200 microplate spectrophotometer (Biochrom) at 450 nm.

doi:10.1038/nm.4133

***Ex vivo* restimulation of splenocytes and T cells with *E. coli*.** Spleens from VTA-activated mice and their controls were processed, and cells were incubated with heat-killed *E. coli* for 72 h (10^6 c.f.u./ml co-cultured with 10^6 splenocytes, 37 °C, 5% CO_2). We then analyzed, using flow cytometry, IgG (polyclonal goat anti-mouse IgG; SouthernBiotech; detected with Alexa-Fluor-488-conjugated streptavidin, Jackson) levels on B cells. We isolated T cells using negative selection (EasySep mouse T cell isolation kit; Stemcell Technologies). To reactivate the T cells, we incubated them with activated macrophages from a naive group of mice that were exposed to *E. coli* 48 h earlier (10^6 macrophages co-cultured with 10^6 T cells, 37 °C, 5% CO_2). Three days later, we analyzed the intracellular T cell IFN-γ expression, using flow cytometry as described above.

Delayed-type hypersensitivity (DTH) response. 24 h after CNO injection, we i.p. injected 1.5×10^7 c.f.u. of heat-killed *E. coli* (150 µl in sterile PBS). Thirty days later, the mice were challenged subcutaneously with 5×10^6 c.f.u. of heat-killed *E. coli* emulsified with incomplete Freund's adjuvant (Sigma-Aldrich). Swelling was measured with a digital caliper 72 h later. Then, the mice were killed, and the adjacent lymph nodes were extracted for analysis.

Sympathetic denervation. Virus-injected mice (30 d after stereotactic injection) were sympathetically denervated by two i.p. injections of 6-OHDA (150 mg/kg in 0.01% ascorbic acid; Sigma-Aldrich) administered at 24-h intervals. Mice were injected i.p. with CNO 5 d after the last 6-OHDA injection and, 24 h later, spleens were removed and homogenized for evaluation of norepinephrine levels (using competitive ELISA based on the manufacturer's instructions; IBL). Spleens from other groups of mice were used for CyTOF analysis or *ex vivo E. coli* killing assays.

Statistical analysis. Analysis of CyTOF data is described in the 'Citrus analysis of CyTOF data' section. In all other experiments, significance levels of other data were determined by using Prism5 (GraphPad Software). Experiments were analyzed by two-tailed Student's *t*-test, or by one-way or two-way analysis of variance (ANOVA), as indicated for each experiment. Experiments were done twice.

33. National Research Council. *Guide for the Care and Use of Laboratory Animals* 8th edn. (The National Academies Press, 2011).
34. Lammel, S. *et al.* Diversity of transgenic mouse models for selective targeting of midbrain dopamine neurons. *Neuron* **85**, 429–438 (2015).
35. Rogan, S.C. & Roth, B.L. Remote control of neuronal signaling. *Pharmacol. Rev.* **63**, 291–315 (2011).
36. Bruggner, R.V., Bodenmiller, B., Dill, D.L., Tibshirani, R.J. & Nolan, G.P. Automated identification of stratifying signatures in cellular subpopulations. *Proc. Natl. Acad. Sci. USA* **111**, E2770–E2777 (2014).
37. Parmigiani, G., Garrett, E.S., Anbazhagan, R. & Gabrielson, E. A statistical framework for expression-based molecular classification in cancer. *J. R. Stat. Soc. Series B Stat. Methodol.* **64**, 717–736 (2002).
38. Heller, E.D., Leitner, H., Drabkin, N. & Melamed, D. Passive immunization of chicks against *Escherichia coli*. *Avian Pathol.* **19**, 345–354 (1990).

SUPPLEMENTARY INFORMATION

Activation of the reward system boosts innate and adaptive immunity

Tamar L. Ben-Shaanan[1,2], Hilla Azulay-Debby[1,2], Tania Dubovik[1], Elina Starosvetsky[1], Ben Korin[1,2], Maya Schiller[1,2], Nathaniel L. Green[1,2], Yasmin Admon[1], Fahed Hakim[1,3], Shai S. Shen-Orr[1,4#*], Asya Rolls[1,2#*]

Affiliations:

(1) Department of Immunology, Rappaport Faculty of Medicine, Technion - Israel Institute of Technology, Haifa, Israel.

(2) Center of Science and Engineering of Neuronal Systems, Rappaport Faculty of Medicine, Technion - Israel Institute of Technology, Haifa Israel.

(3) Pediatric Pulmonary Unit, Rambam Health Care Campus, Haifa, Israel.

(4) Faculty of Biology, Technion – Israel Institute of Technology, Haifa, Israel.

Supplementary Table S1: Effects of VTA activation replicated in all three repeats of the experiments.

	B cells- CD80	MAC- CD80
Experiment #1	30.51	53.25
Experiment #2	60.66	12.81
Barcoded Experiment	68.04	5.31

	B cells- CD86	MAC- CD86
Experiment #1	27.08	20.69
Experiment #2	36.87	6.97
Barcoded Experiment	19.41	44.53

	B cells- TLR4	MAC- TLR4
Experiment #1	37.54	15.10
Experiment #2	2.19	53.47
Barcoded Experiment	13.29	11.43

	B cells- CD25
Experiment #1	30.12
Experiment #2	25.54
Barcoded Experiment	40.71

Experiment #1-2 with non-barcoded data (n=5 mice per group) and an additional experiment, evaluated by barcoding (n=3 VTA activated and 5 controls). Significant differences are reported as a percentage of increase in the expression intensity in the VTA-activated group compared to the control group. Of note, we provide in Figure S3 and S4 the specific details of one representative experiment done without barcoding and in Table S1, we provide a summary of the effects replicated in all three experiments including the barcoded data. Thus, for example, we did not identify differences in DCs in the barcoded experiment and, therefore, we do not refer to these cells in the text.

Table S2: CyTOF antibody panel.

Isotope	Ab	Clone Catalog no.	Experiment	Use
(In115)Di	CD45	30-F11 103120	● ● ● ●	C
(La139)Di	CCR3	JO73E5 144504	● ● ●	C, F
(Pr141)Di	CD80	16-10A1 104702	● ● ● ●	F
(Nd142)Di	GR1	RB6-8C5 108402	● ● ● ●	C, A
(Nd143)Di	CD86	GL-1 105002	● ● ● ●	F
(Nd144)Di	F4/80	BM8 123102	● ● ● ●	C, A
(Nd145)Di	CD4	RM4-5 100520	● ● ● ●	C, A
(Nd146)Di	CD45R	RA3-6B2 103202	● ● ● ●	C, A
(Sm147)Di	CD152	3C7 106202	● ● ●	F
(Nd148)Di	CD138	281-2 142502	● ● ● ●	F
(Sm149)Di	CD8	53-6.7 100716	● ● ● ●	C, A
(Nd150)Di	NK1.1	PK136 108702	● ● ● ●	C, A
(Eu151)Di	CD206	C068C2 141702	● ● ● ●	C, F
(Sm152)Di	CD25	3C7 101902	● ● ● ●	C, F
(Eu153)Di	CD14	Sa14-2 123302	● ● ● ●	C, A
(Sm154)Di	CD11c	N418 117302	● ● ● ●	C, A
(Gd155)Di	IgM	RMM-1 406502	● ●	C, F
(Gd156)Di	CD49b	DX5 108902	● ● ● ●	C, A

C = Clustering
F = Function
A = Cell-subset annotation
NA = Not analysed

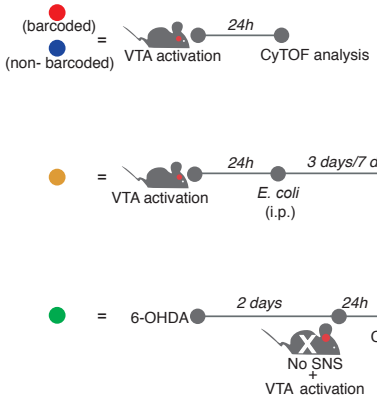

Isotope	Ab	Clone Catalog no.	Experiment	Use
(Gd157)Di	CD19	6D5 115502	● ●	C
(Gd158)Di	CD34	MEC14.7 119302	● ● ● ●	C
(Tb159)Di	CD27	LG.3A10 124202	● ● ● ●	F
(Gd160)Di	CD69	H1.2F3 104502	● ● ● ●	F
(Dy161)Di	CD123	5B11 106002	● ● ●	NA
(Dy162)Di	TCRb	H57-597 109202	● ● ● ●	C, A
(Dy163)Di	CCR7	4B12 120101	● ● ●	F
(Dy164)Di	CD28	37.51 102102	● ● ● ●	F
(Ho165)Di	CD115	AFS98 135502	● ● ● ●	F
(Er166)Di	CD133	315-2C11 141202	● ● ● ●	C
(Er167)Di	TLR4	SA14-21 145402	● ● ● ●	F
(Er168)Di	CD117	ACK2 135102	● ● ● ●	C
(Tm169)Di	CD79b	HM79-12 132802	● ● ● ●	C, A
(Er170)Di	CD62L	MEL-14 104402	● ● ● ●	C
(Yb171)Di	CD44	IM7 103033	● ● ● ●	C
(Yb173)Di	TLR2	T2.5 121802	● ●	F
(Yb173)Di	CD45RA	14.8 sc-18865	● ●	NA
(Yb174)Di	IA-IE	M5/114.15.2 107602	● ● ● ●	C, F
(Lu175)Di	IgD	11-26c.2a 405737	● ●	F
(Yb176)Di	CD11b	M1/70 101202	● ● ● ●	C, A

Isotope	Ab	Clone Catalog no.	Experiment	Use
(Sm147)Di	CD3e	145-2C11 100314	●	C, A
(Dy161)Di	CD21	7E9 123404	●	F
(Dy163)Di	CD127	A7R34 135002	●	F
(Yb172)Di	CD23	B3B4 101625	●	F

The antibodies used for clustering (C), annotation (A) and functional (F) analysis of the immune populations are shown with the clone details and the CyTOF channels for each antibody. Markers discarded from the analysis altogether are marked NA (not analyzed). Clustering was performed with Citrus based on similarity of expression of all clustering markers. The antibodies used in each panel are specified with a color code. All antibodies were purchased from BioLegend, except CD45RA that was purchased from Santa-Cruz Biotechnology. All antibodies were validated by the manufacturer's for flow application as indicated on the manufacturer's website

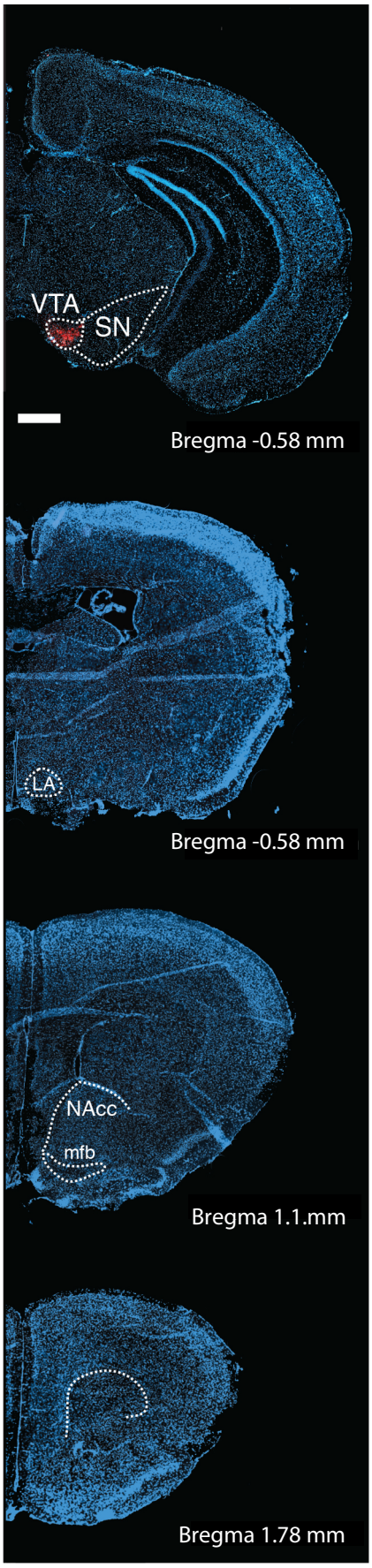

Supplementary Figure 1: DREADD expression in the VTA. Coronal sections of a virus-infected brain evaluating mCherry labeling in the ventral tegmental area (VTA), substantia nigra (SN), lateral hypothalamus (LA), nucleus accumbens (NAcc), medial forebrain bundle (mfb) and the frontal cortex. mCherry expression is evident only within the VTA. Blue-DAPI, red-mCherry. Scale bar, 0.5 mm

Nature Medicine: doi:10.1038/nm.4133

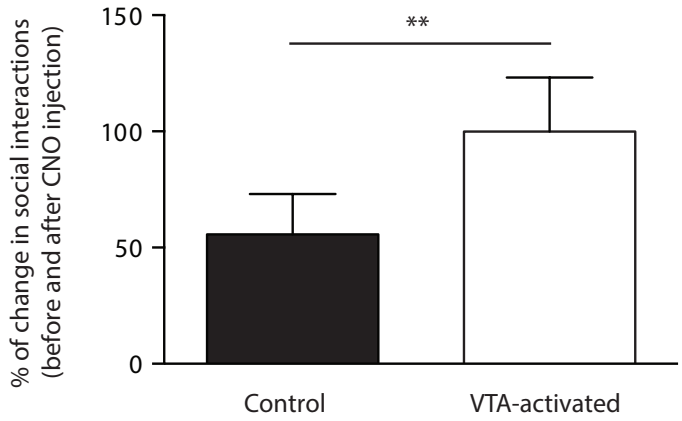

Supplementary Figure 2: DREADD-induced VTA activation increases social interaction. DREADD-induced VTA-activation increased the number of social interactions between cage mates. ($n = 5$; $P < 0.01$). Data represented as mean ± s.e.m.

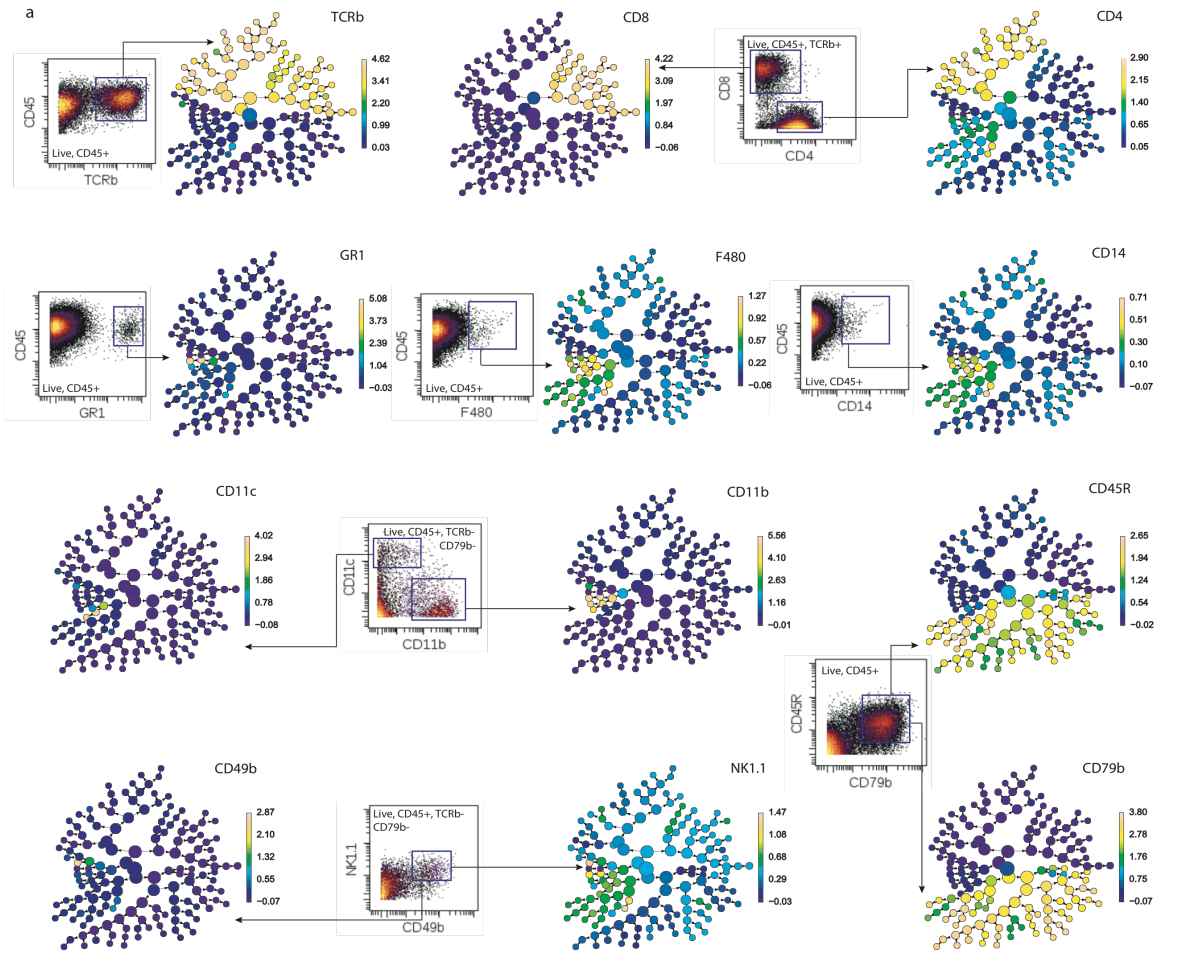

Nature Medicine: doi:10.1038/nm.4133

Supplementary Figure 3: VTA-activation induces small but specific changes in immune populations. Spleens from VTA-activated and control mice were subjected to analysis by CyTOF mass cytometry (n = 5 per group; experiment #1 in Table S1). The identified cell clusters are represented as nodes in a Citrus derived circular dendrogram delineating lineage relationships as identified from the data. Cluster granularity (*i.e.* cell subset specificity) increases from the center of the diagram to the periphery. **(a)** The expression intensity of each marker used for cell population characterization is overlaid per cluster on the Citrus circular dendrogram and is indicated, independently for each marker, by the colored gradient whose range corresponds to the *arcsinh* transformed expression of the median marker expression measured across all Citrus clusters. For each marker we also provide a dot plot graph demonstrating the marker labeling in the manually gated indicated population. **(b)** Citrus plots showing, per marker, the clusters (pink) for which testing of group differences was restricted to based on an unsupervised application of a Probability of Expression (POE) algorithm. Shown is the POE information for the six markers in which group differences were identified, **(c)** Citrus plots delineating lineage relationships as identified from the data and group differences. Individual cell clusters are mapped to well established, gross-cell types: B cells ($CD45R^+CD79b^+$), $CD8^+$ T cells ($TCR\beta^+CD8^+$), $CD4^+$ T cells ($TCR\beta^+CD4^+$), NK cells ($NK1.1^+CD49b^+$), granulocytes ($CD11b^+Gr\text{-}1^+$), monocytes/macrophages ($CD11b^+CD14^+F4/80^+$) and dendritic cells (CD11c+) identifiable by annotated shaded background groupings. Cell subsets, not well defined by these criteria were left white. Differences in functional markers' expression for cell clusters in the spleen of VTA-activated and control mice are indicated for each cell cluster by one or more colored rings, corresponding to different functional markers, in which the median expression is different between the two experimental groups. Changes are shown for CD80, CD86 and MHCII (left) and CD25, CD115 and TLR4 (right).

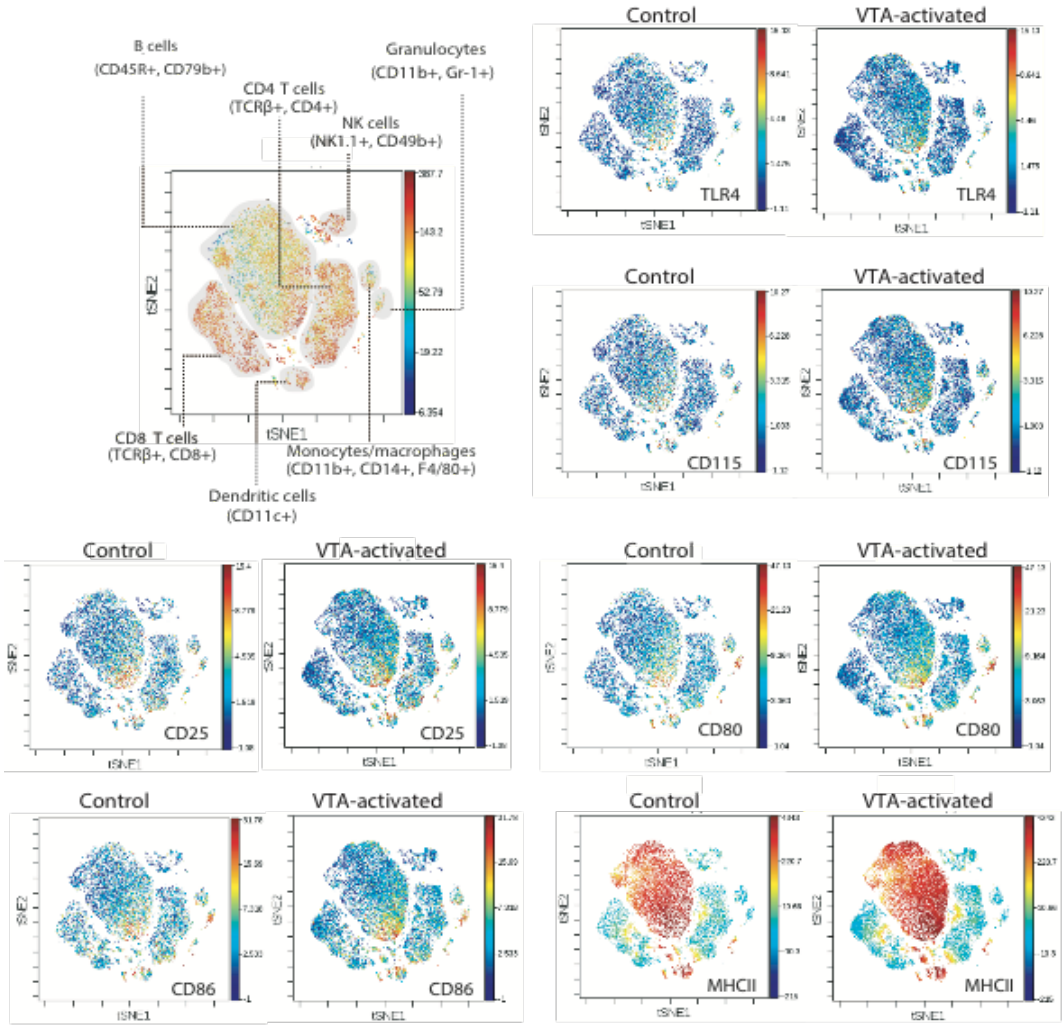

Supplementary Figure 4: ViSNE dimensionality reduction reveals subtle upregulation of protein expression in immune subpopulations. CyTOF analysis of VTA activated and control mice (n = 5 per group, same experiment shown in **Supplementary Figure 3**) was analyzed using ViSNE, an orthogonal analysis paradigm to Citrus, which relies on a non-linear dimensionality reduction to two dimensions of single cell distances (measured on the same markers used for clustering in the Citrus analysis). On the upper left, is a ViSNE plot, colored for CD45 marker expression with ViSNE "islands" annotated to gross cell-types. Additional plots provide the baseline comparison ViSNE representation of TLR4, CD115, CD25, CD80, CD86 and MHCII median expression levels in control and VTA-activated mice. Color code indicates expression intensity.

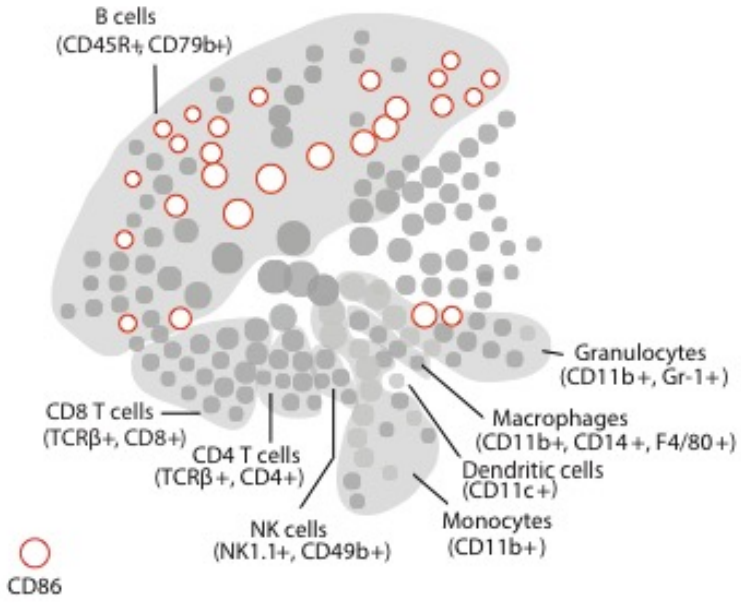

Supplementary Figure 5: Changes in blood cells following VTA activation. Blood cells from VTA-activated mice and controls were assayed by CyTOF followed by Citrus clustering and analysis of group differences. Clusters represented as nodes in a Citrus-derived circular dendrogram. Individual cell clusters are mapped to well established, gross-cell types, identifiable by annotated shaded grey background groupings, with cluster granularity (i.e. cell subset specificity) increasing moving from the center of the diagram to the periphery. Colored clusters represent an increase in median expression of CD86 (n = 5 and 7).

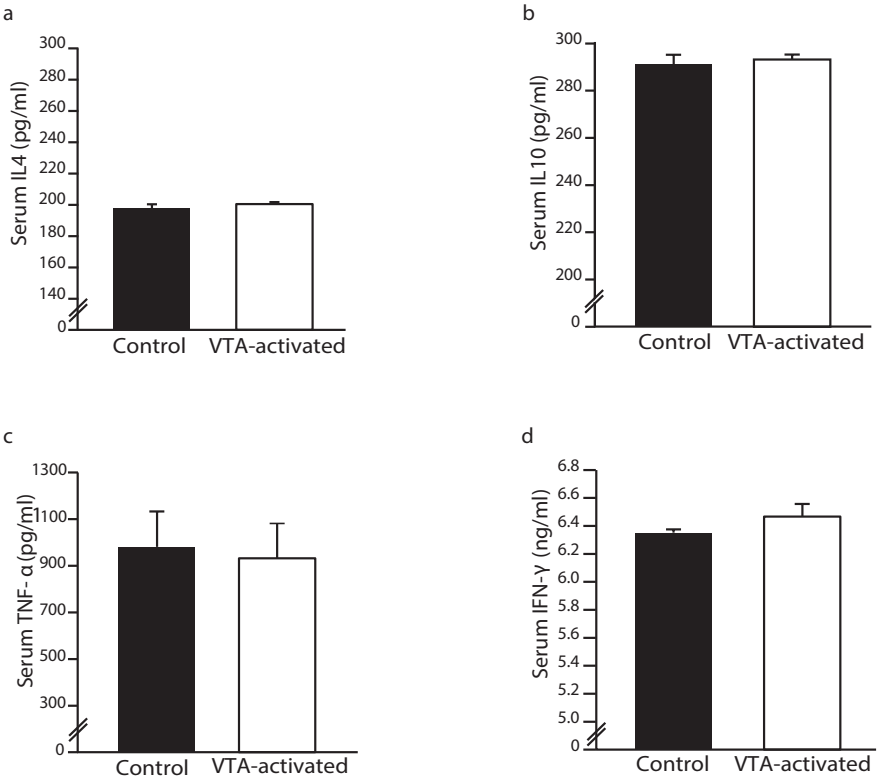

Supplementary Figure 6: VTA activation does not induce changes in mouse serum cytokines. Serum samples of VTA-activated and control mice were analyzed for their cytokines levels using standard ELISA kits. The results are reported following background subtraction and calculation of pg or ng /ml levels of each cytokine (n = 6). Data represented as mean ± s.e.m.

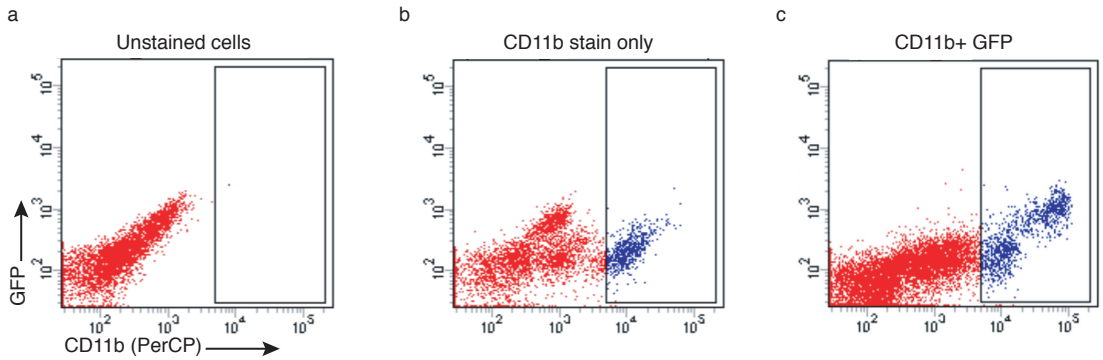

Supplementary Figure 7: Validation of GFP fluorescence on peritoneal CD11b+ cells. Validation of the GFP levels of peritoneal CD11b+ cells from mice infected with non-fluorescent *E. coli* or GFP-*E. coli.* (**a**) Peritoneal unstained cells two hours following *i.p.* injection of non- fluorescent *E. coli*. (**b)** Peritoneal cells two hours after *i.p.* injection of non-fluorescent *E. coli* stained with anti CD11b PerCP conjugated antibody. (**c)** Peritoneal cells two hours after i.p. injection of GFP-expressing *E. coli* stained with anti CD11b PerCP conjugated antibody. $CD11b^{high}$ cells show increased levels of GFP only after infection with GFP-expressing bacteria.

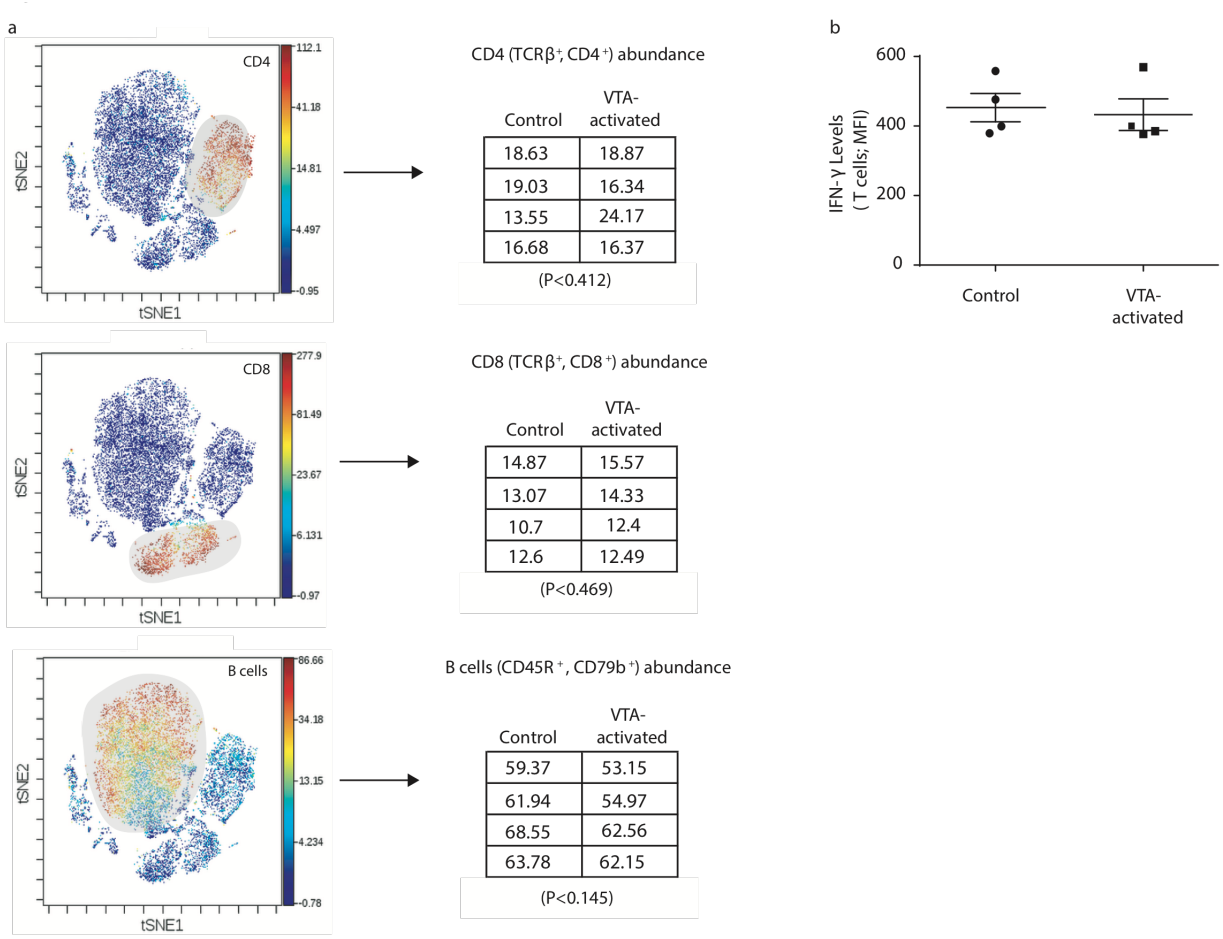

Supplementary Figure 8: CyTOF and Flow cytometry analyses of splenocytes seven days after *E. coli* challenge reveal similar pattern of activation in control and VTA-activated mice. (**a**) CyTOF analysis of the changes in splenocytes derived from VTA-activated mice and their controls seven days following *E. coli i.p.* injection. CyTOF data using ViSNE analysis is represented on the left panel. The percentage of abundance for each population is provided in the right panel for each mouse. The gating strategy of the different cell subsets is demonstrated on a representative mouse. (**b**) Intracellular IFN-γ expression represented as median fluorescence intensity (MFI) of spleen T cells from VTA activated mice and their controls (n = 4). Data represented as mean ± s.e.m.

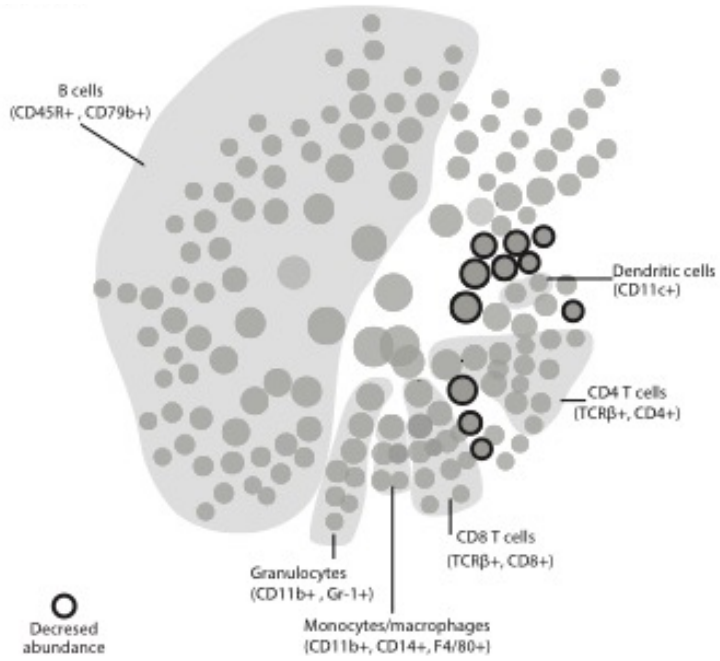

Supplementary Figure 9: VTA activation has no effect on the immune system in sympathetically-ablated mice. To evaluate the impact of VTA activation in the absence of SNS, we compared the CyTOF analysis between two groups of mice, both treated with 6-OHDA. Cell clusters are represented as nodes in a circular dendrogram delineating lineage relationships as identified from the data. Individual cell clusters are mapped to well established, gross-cell types, identifiable by annotated shaded grey background groupings, with cluster granularity (i.e. cell subset specificity) increasing moving from the center of the diagram to the periphery. Cell clusters that demonstrated change in cell abundance are circled in grey. The observed changes were mainly in cell clusters that could not be characterized, as they did not express any of the cell-type markers used in the assay. No other differences were detected even at FDR 50%. We repeated the experiment two independent times, with qualitatively similar results (n = 6 and 8).

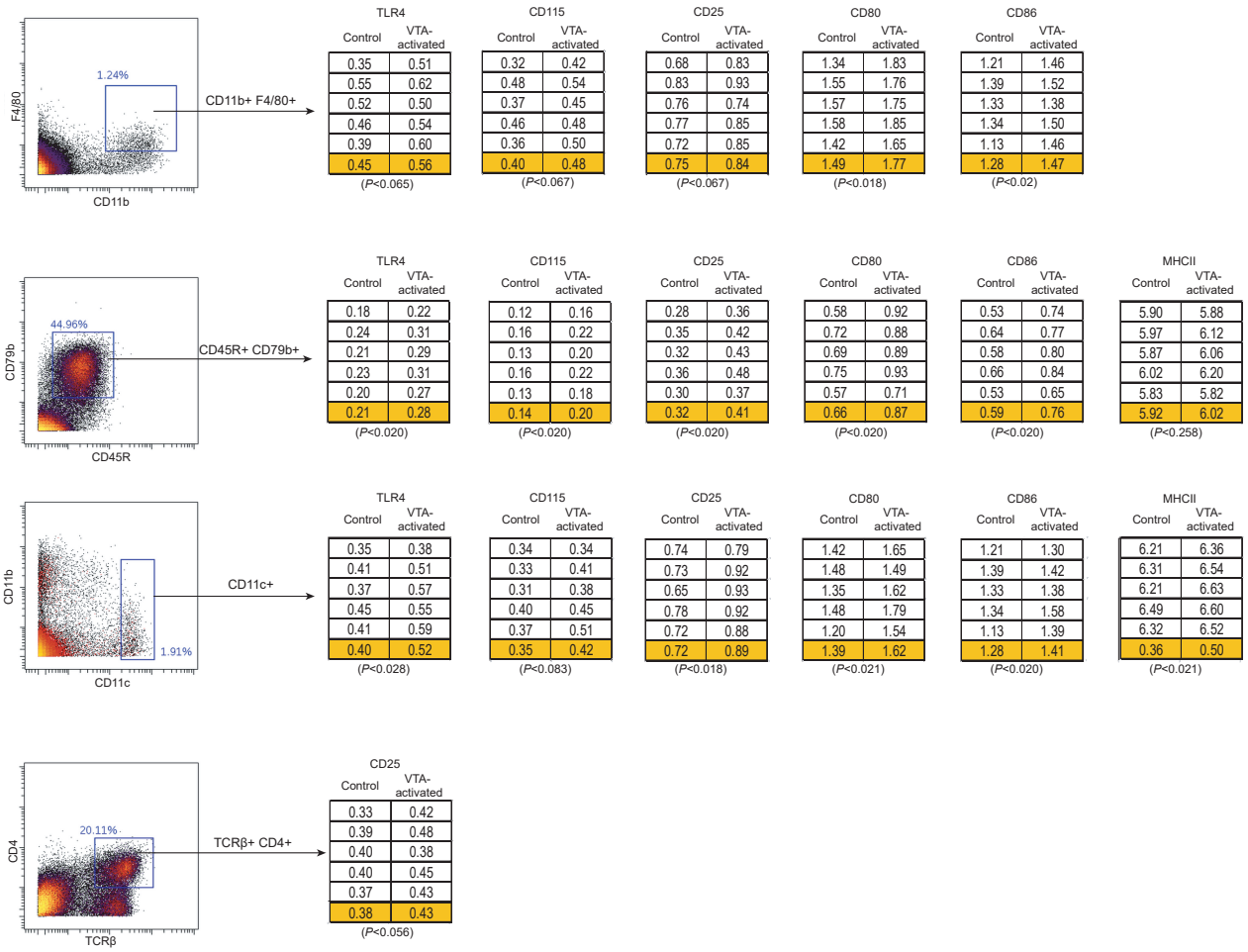

Supplementary Figure 10: Manually gated single cell CyTOF data and effect size of functional marker differences. Broad manual gates of single cell CyTOF data are shown for the key populations (macrophages, B-cells, dendritic cells and CD4 T-cells) in which the Citrus-based analysis identified differences between naive VTA-activated and control mice in a single independent experiment (experiment #1 of Table S1). Median (arcsinh transformed) functional marker intensity values are shown for TLR4, CD115, CD25, CD80, CD86 and MHCII in each mouse, as well as a Student *t*-test Benjamini-Hochberg adjusted *p*-value for group differences. The gating strategy is demonstrated on a single mouse.

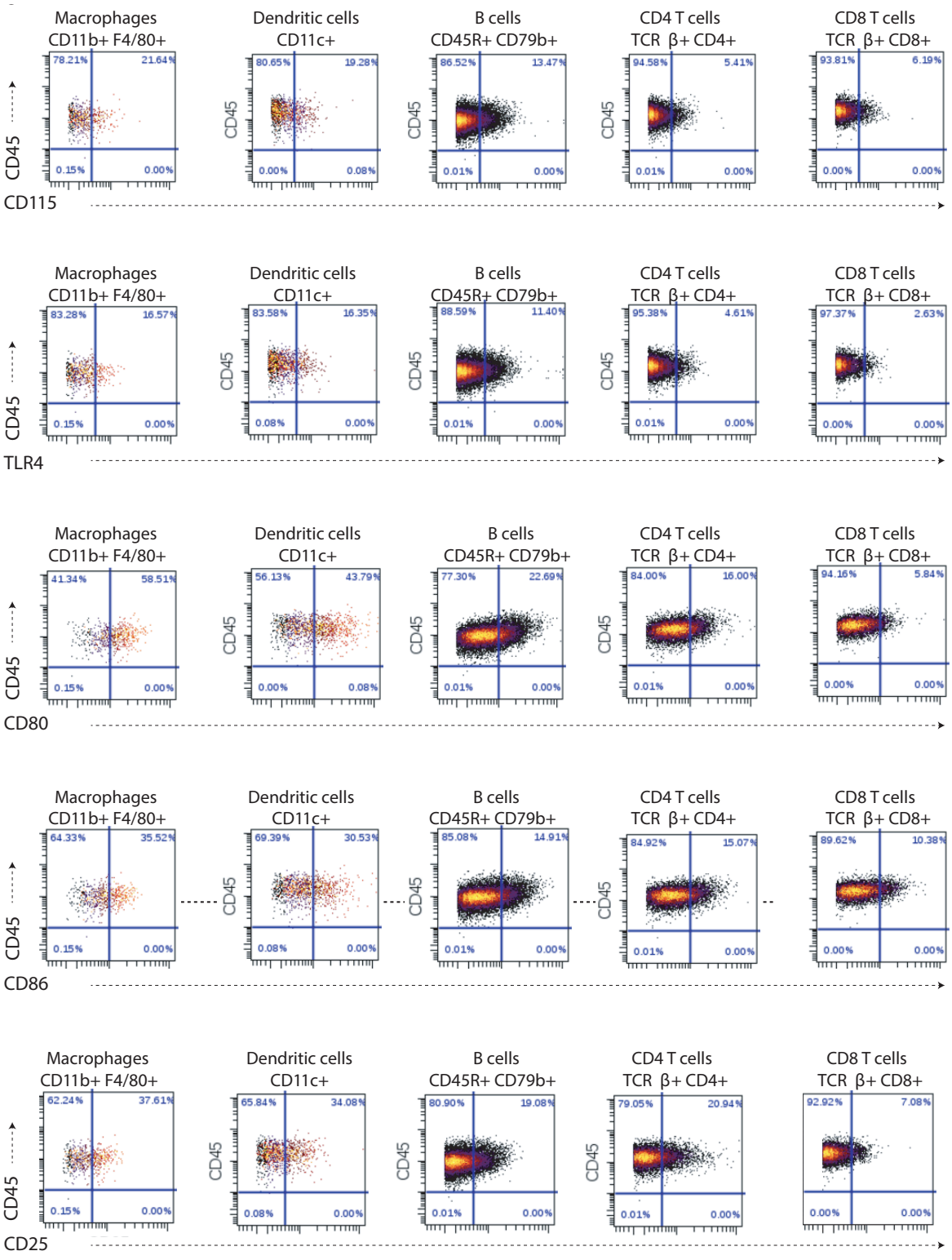

Supplementary Figure 11: Expression pattern of low intensity markers affected by VTA activation across immune populations. Single cell dot plots representing CD115, TLR4, CD80, CD86, and CD25 expression of different immune populations as indicated above each panel in immunologically naïve mice. The scale of marker intensity is adjusted for each marker as indicated.

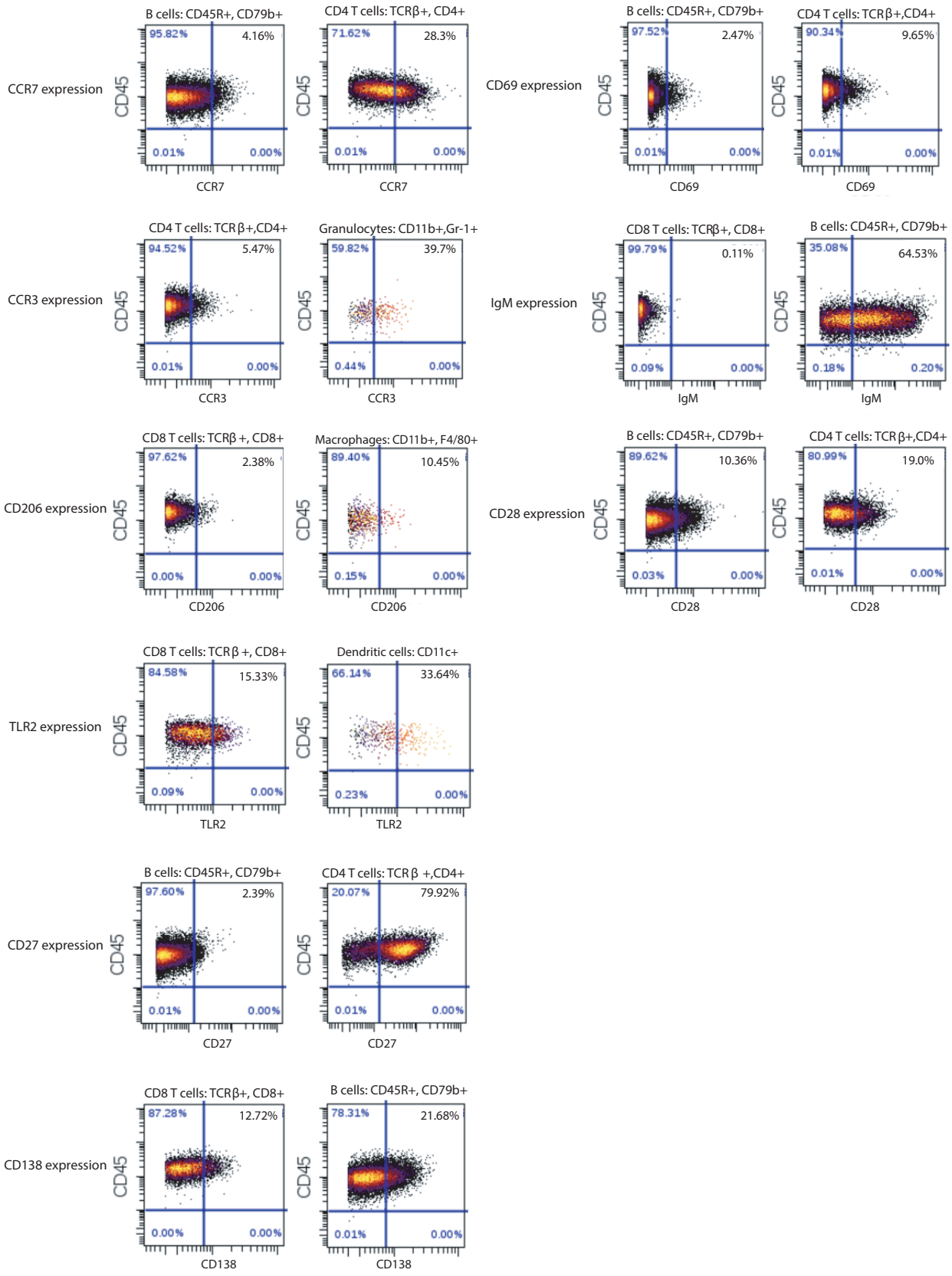

Supplementary Figure 12: Single cell CyTOF data demonstrating marker reliability. *Arcsinh* transformed CyTOF single cell data shown for all pertinent functional markers not affected by VTA-activation, in immunologically naïve mice.

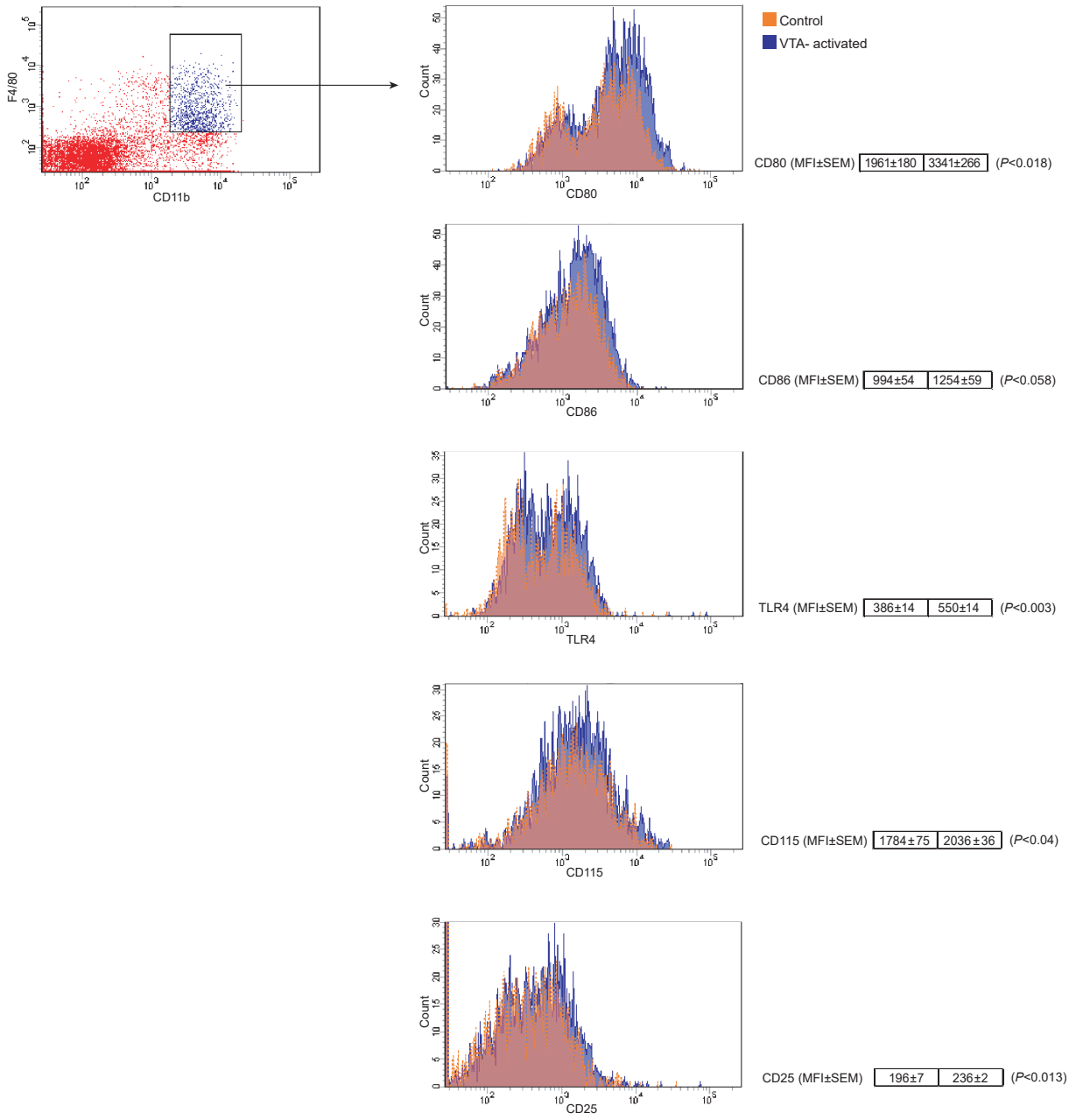

Supplementary Figure 13: Flow cytometry validation of VTA-activation effects on the expression of CD80, CD86, TLR4, CD115 and CD25 on monocytes and macrophages. We isolated monocytes/macrophages from the spleens of VTA-activated mice and their controls 24h after CNO injection. We labeled the cells with fluorescently labeled antibodies to CD11b, F4/80, CD80, CD86, TLR4, CD115 and CD25. The cells were then analyzed by flow cytometry for the expression of these markers of cells gated based on the CD11b, F4/80 staining as demonstrated in the left panel. In the right panels, representative histograms are shown. The average MFI ± s.e.m. per group are shown. As each marker was analyzed individually, p values were evaluated by student's *t*- test (n = 3 mice per group).